

Design Concept of Co-ionic Conducting Solid Oxide Electrolyte for Stable Operation in a Cell-imbalanced Fuel Cell Stack

Atif Khan Niaz^{1†}, Young Je Kim^{2†}, Anil. V. Virkar³, Jun-Young Park⁴, Hyung-Tae Lim^{1,2,3*}

¹School of Materials Science and Engineering, Changwon National University,
Changwon, Gyeongnam 51140, Republic of Korea

²Department of Materials Convergence and System Engineering, Changwon National
University, Changwon, Gyeongnam 51140, Republic of Korea

³Department of Materials Science and Engineering, University of Utah, Salt Lake City,
Utah 84112, USA

⁴HMC & Green Energy Research Institute, Department of Nanotechnology and Advanced
Materials Engineering, Sejong University, Seoul 05006, Republic of Korea

*Corresponding author. Tel: +82-55-213-3716; Fax: +82-55-262-6486

E-mail address: hraelim@changwon.ac.kr

† Both authors contributed equally to this work.

ABSTRACT

A bilayer composite electrolyte comprising BaCe_{0.85}Y_{0.15}O_{3-d} (BCY15) – Gd_{0.2}Ce_{0.8}O_{2-d} (GDC20) at the anode side and BaZr_{0.85}Y_{0.15}O_{3-d} (BZY15) – Nd_{0.1}Ce_{0.9}O_{2-d} (NDC10) at the cathode side is designed for improving the stability of co-ionic conducting solid oxide fuel

cells (SOFCs) in a cell imbalanced stack. Contrary to the single layer structured SOFCs, the bi-layer cell stably operates without electrode delamination under negative voltage conditions. We measure local internal p_{O_2} values using embedded Pt probes. Based on these values, local electronic conduction is estimated in combination with four probe DC conductivity measurements. It is found that n-type conductivity ($\sim 10^{-3} \text{ Scm}^{-1}$) and p-type conductivity ($10^{-5} \sim 10^{-4} \text{ Scm}^{-1}$) are developed in the BCY15-GDC20 near the anode side and in the BZY15-NDC10 near the cathode side, respectively. The results indicate that local electronic conduction in electrolyte regions near both the anode and cathode interfaces is a crucial factor for the durability of co-ionic SOFCs under negative voltage operation. We therefore suggest the bi-layer configuration as a practical solution to protect co-ionic SOFCs in a cell-imbalanced stack.

Key words: *Solid oxide fuel cells, Co-ionic conduction, Composite electrolyte, Cell imbalance, Durability*

I. INTRODUCTION

Solid oxide fuel cells (SOFCs) are highly efficient energy conversion (chemical energy to electrical energy) devices having minimum environmental impact with lower emissions of pollutants as compared to other power generating systems. Recently, decreasing the operating temperature of SOFCs has been at the center of intense research endeavors [1]. A conventional SOFC electrolyte, yttria stabilized zirconia (YSZ), is operated at relatively high temperature of ~ 800°C due to the high activation energy of oxygen ion transport. The high operating temperature brings about advantages including high-energy efficiency and circumventing the need for precious metals. [2]. On the other hand, it causes thermal degradation issues such as coarsening of particles in the electrodes and chemical interactions between stack components [3, 4].

Doped ceria (CeO_2) has been reported to be one of the promising electrolytes for intermediate SOFCs (500 ~ 700°C). However, ceria is chemically unstable under a reducing atmosphere, giving rise to mixed ionic electronic conduction that eventually lowers the open circuit voltage and output power density [5]. Researchers have developed doped ceria – alkali carbonate composite electrolytes for higher ionic conductivity and ionic transference number compared to doped ceria. However, these composite electrolytes have issues such as low chemical stability under moisture and high temperature conditions [6, 7]. Another class of low temperature SOFC electrolytes is proton conducting perovskite oxides, such as doped barium cerates (BaCeO_3), doped barium zirconates (BaZrO_3) and their solid solution, which have a high ionic conductivity at an intermediate temperature regime [8]. Doped BaCeO_3 has a higher proton conductivity compared to doped BaZrO_3 , but it has poor chemical stability under CO_2 and H_2O environments [9]. Doped BaZrO_3 is chemically stable, but its grain boundary resistance is

significant because of the poor sinterability. [10, 11]. Recently, a co-ionic conducting electrolyte model was put forward, comprising a composite of oxygen ion conducting ceria and a proton conducting perovskite oxide to prevent leakage currents, improve the CO₂ and H₂O tolerance, and alleviate fuel dilution [12-21]. However, research groups have not adequately addressed the stability of co-ionic conducting SOFCs under severe operating conditions in a stack level, which should be considered for their commercialization. Cell to cell performance variation (cell imbalance) may bring about catastrophic failure in a series-connected electrochemical device [22-24]. This phenomenon is well known in lithium-ion battery systems; electrical abuse (over-charging/discharging) associated with cell imbalance may lead to thermal runaway [25]. In the case of a fuel cell stack, a bad cell with higher resistance can operate at a negative voltage, and its electrolyte/electrode interface can be delaminated by high partial pressured developed in the electrolyte, eventually resulting in stack failure [14, 26, 27]. This is known as ‘electro-chemo-mechanical failure (electrochemically induced mechanical failure)’ and is one of the significant issues addressed in all-solid-state secondary batteries and solid oxide electrolysis cells [28, 29]. Stack monitoring and a management system are required for protecting stacks and expanding their lifespan, but it is more important to develop SOFCs that stably operate even at a negative voltage.

In our previous study on co-ionic conducting composite electrolytes, we found that BCY15 (BaCe_{0.85}Y_{0.15}O_{3-d}) - GDC20 (Gd_{0.2}Ce_{0.8}O_{2-d}) and BZY15 (BaZr_{0.85}Y_{0.15}O_{3-d}) - NDC10 (Nd_{0.1}Ce_{0.9}O_{2-d}) cells were stable at positive cell voltages, but both readily degraded upon being subjected to negative cell voltages [14]. It was observed that electrolyte regions with higher electronic resistance (a region close to the anode side for BZY15-NDC10 and a region close to the cathode side for BCY15-GDC20) were physically damaged (delaminated) during negative voltage tests. On the other hand, we did not observe any damage on the relatively high

electronic conducting regions (a region close to the cathode side for BZY15-NDC10 and a region close to the anode side for BCY15-GDC20) after negative voltage tests. These results indicate that electrolyte/electrode interfaces can be protected from physical damage by stabilizing the internal partial pressure with some degree of electronic conduction in the electrolyte. On the basis of a local equilibrium assumption, we can write the relationship between the internal oxygen chemical potential (partial pressure) and the electronic concentration in an electrolyte as follows [26]:

$$\mu_{O_2} = 2\tilde{\mu}_{O^{2-}} - 4(\mu_e^0 + RT\ln C_e - e\Phi) \quad (1)$$

where μ_{O_2} is the chemical potential of oxygen; $\tilde{\mu}_{O^{2-}}$ is the electrochemical potential of oxygen ions; μ_e^0 is the chemical potential of electrons in a standard state; R is the gas constant, T is the temperature; C_e is the electronic concentration; e is the elementary charge; and Φ is the local electrostatic potential. This equation suggests that the higher the electronic concentration is, the lower the internal partial pressure will be. An anode/electrolyte interface should be protected in oxygen ion conducting SOFCs while a cathode/electrolyte interface must be protected in proton conducting SOFCs [10, 27]. In the case of co-ionic conducting SOFCs in which protons and oxygen ions are transported from the anode to the cathode and vice versa, respectively, local electronic conduction is required in electrolyte regions near both electrode sides to circumvent electrochemically induced mechanical failure issues. From this perspective, we modified composite electrolytes by designing a bi-layer structure in the present study: BCY15-GDC20 and BZY15-NDC10 were placed at the anode (for n-type conduction) and at the cathode sides (for p-type conduction), respectively. Effects of the bi-layer structure on improving stability were evaluated by subjecting the cell to negative voltages. Embedded Pt

probes were utilized to measure internal partial pressures in the electrolyte region near the anode and cathode sides. Based on the measured internal partial pressures, local electronic conductivities were determined in combination with four probe DC conductivity measurements. This study suggests a new concept of co-ionic conducting composite electrolyte design for stable operation in a cell imbalanced stack.

II. EXPERIMENTAL PROCEDURE

Anode supported bi-layer electrolyte SOFCs were fabricated as follows. Two kinds of composite electrolytes, BCY15-GDC20 in 65:35 wt% and BZY15-NDC10 in 25:75 wt%, were prepared in the same manner as described in our previous work [14]; we maintained the same dopants and the same weight ratio of proton conductor to oxygen ion conductor as in our previous work. Maintaining the same material conditions as employed previously, we could see solely the effects of the bi-layer structure on the cell stability under negative voltage conditions. An anode support (AS) was prepared by die-pressing a NiO+ BaCe_{0.7}Zr_{0.1}Y_{0.1}Yb_{0.1}O_{3-δ} (BCZYYb) powder (65 wt% + 35 wt%), and then fired at 950°C. An anode functional layer (AFL) was deposited on the AS using a NiO+ BCY15-GDC20 slurry (60 wt% + 40 wt%), and then fired at 950°C. The first electrolyte layer was prepared by drop coating a BCY15-GDC20 slurry on the AFL. A Pt probe was embedded in the first electrolyte, which is denoted as 'Ref#2'. The method of embedding Pt probes and attaching lead wires to probes can be found elsewhere [30]. After firing the first electrolyte at 1000°C, the second electrolyte of BZY15-NDC10 was deposited using drop coating. Another Pt probe was embedded in the second electrolyte. This embedded probe is denoted as 'Ref#1'. The anode supported bi-layer was sintered at 1550°C for 4 h. A cathode functional layer (CFL) of NdBa_{0.5} Sr_{0.5} Co_{1.5}Fe_{0.5}O_{5.5} (NBSCF)+NDC10 (60 wt% + 40 wt%) was deposited on the bi-

layer, followed by a firing process at 1150°C. A schematic diagram and a photograph of the Pt probe-embedded bi-layer cell are shown in Figures 1(a) and (b), respectively. We prepared 'Pt probe-free' bi-layer cells for material analyses and durability tests. Note that the electrolyte thickness of the 'Pt probe-free' cell (20~30 μm) was much smaller than that of the 'Pt probe embedded' cell (~ 40 μm). Scanning electron microscopy (SEM) with energy dispersive spectroscopy (EDS) line scanning and x-ray diffraction (XRD) analyses were carried out on the fabricated bi-layer cell.

A specially designed test fixture was used for electrochemical performance tests [31]; hydrogen and air were supplied to the anode and the cathode sides, respectively, at a flow rate of 300 mLmin⁻¹. I-V characteristics and impedance spectra were evaluated using a Bio-Logic SP 240 potentiostat/galvanostat. Durability tests were conducted by subjecting the cell to a positive voltage (~ 2 h) followed by a negative voltage (~ 90 h). Voltage between the cathode and 'Ref#1' and between the anode and 'Ref#2' was measured in the Pt probe-embedded cells under open circuit conditions at 600 °C. Based on these measurements, internal partial pressure at the probe location was determined. We prepared bar shaped samples of BCY15-GDC20 and BZY15-NDC10, which were sintered at the same sintering temperature for the anode supported bi-layer cell. Pt electrodes were painted on the bar samples for four probe DC conductivity measurement. Their electrical conductivity was measured using a Keithley DMM6500 at 600°C at various partial pressures of oxygen (p_{O_2}). From conductivity data as a function of p_{O_2} , we determined electronic conductivities in the region near the anode interface of the BCY15-GDC20 electrolyte and the region near the cathode interface of the BZY15-NDC10 electrolyte.

III. RESULTS AND DISCUSSION

Figure 2(a) compares XRD patterns of BZY15, NDC10, BCY15, and GDC20 powders, and bi-layer electrolytes fired at 500 °C and sintered at 1550°C. Note that 2- theta peak positions were slightly different for BZY and BCY due to different lattice parameters. In the case of the bi-layer fired at 500°C, we observed all the three phases corresponding to BZY15 and BCY15 and doped ceria (NDC10 and GDC20). On the other hand, XRD peaks corresponding to a BCY and BZY solid solution (namely, BCZY) were detected in the bi-layer sintered at a high temperature of 1550°C [11]. Note that no other secondary phases were observed in the sintered bi-layer. Figure 2(b) shows an SEM image of the cross-section of a 'Pt probe free' bi-layer sintered at 1550°C, with the results of EDS line scanning of Zr element. The Zr profile indicated that a bi-layer interface was positioned in the middle of the electrolyte. It was also observed that the Zr concentration slightly decreased from the cathode to the interface within the BZY15-NDC10 layer while it slightly increased from the anode to the interface within the BCY15-GDC20 layer, indicating that Zr of the BZY15-NDC10 was diffused into the BCY15-GDC20. Additionally, EDS spot analyses were carried out for the atomic ratio of Zr to (Zr+Ce) on the bi-layer electrolyte region near the cathode (Figure S1a in the supporting information), and the results were compared with those of a BZY15-NDC10 single layer (Figure S1b). The atomic ratios of Zr to (Zr+Ce) were ~0.12 and ~0.124 for the former and the latter, respectively. Similarly, EDS spot analyses were conducted on the bi-layer electrolyte region near the anode (Figure S1c) and on a BCY15-GDC20 single layer (Figure S1d). The atomic ratios of Zr to (Zr+Ce) were determined to be ~0.046 and ~0 for the former and latter, respectively; a solid solution of $\text{BaCe}_{0.85-x}\text{Zr}_x\text{Y}_{0.15}\text{O}_{3-d}$ with a very small Zr concentration ($x \sim 0.0391$) was formed near the anode side. These results suggest that the chemical composition of the bi-layer electrolyte became increasingly similar to the original

composition of BZY15-NDC10 and BCY15-GDC20 moving closer to the cathode and anode interfaces, respectively. SEM micrographs of 'Ref#1' and 'Ref#2' are shown in Figures 3(a) and (b), respectively. The distance between 'Ref#1' and the CFL and between 'Ref#2' and the AFL was $\sim 16 \mu\text{m}$ and $\sim 14 \mu\text{m}$, respectively. The thickness of the bilayer electrolyte was $\sim 42 \mu\text{m}$. Note that we designed a relatively thick electrolyte to prevent short circuit between the embedded probes.

The basic electrochemical performance of the 'Pt probe free' bi-layer cell was evaluated. Figure 4(a) shows the initial I-V-P curve measured at 600 °C. Open circuit voltage of $\sim 1.0 \text{ V}$ was achieved. This was still lower than the theoretical value, but much higher than that of doped ceria single-phase electrolyte (0.8 \sim 0.9 V at 600 °C) [17, 32, 33]. Thus, we can state that leakage current was substantially suppressed in the composite bi-layer electrolyte as the perovskite oxide phase protected the doped ceria from reduction [14, 15]. The maximum power density was measured as $\sim 101 \text{ mWcm}^{-2}$. This value is lower than that of the BCY15-GDC20 composite electrolyte (single layer) cell, but comparable to that of the BZY15-NDC10 composite electrolyte (single layer) cell [14]. This indicates that the BZY15-NDC10 layer dominated the overall electrochemical performance of the bi-layer cell. Impedance spectra of the bi-layer cell were measured at open circuit voltage and in a frequency range of 200 KHz to 100 mHz. A Nyquist plot is shown in Figure 4(b). Ohmic area specific resistance (ASR) was obtained from the high frequency (28,160 Hz) intersection of the arc on the real axis, which was $\sim 0.75 \Omega\text{cm}^2$. This relatively high ohmic resistance was due to the thick bi-layer electrolyte. Non-ohmic ASR was determined to be $\sim 1.35 \Omega\text{cm}^2$ by subtracting the ohmic ASR from the total ASR. Note that the high non-ohmic ASR was attributed to the large low frequency impedance (11 \sim 0.1 Hz), which was mainly associated with concentration

polarization. The sharp voltage drop at high current densities in Figure 4(a) also indicates large concentration polarization, which might be due to the non-completed NiO reduction and/or the non-optimized anode support microstructure.

After the initial performance test, the bi-layer cell was subjected to positive and negative voltages for ~ 100 h. The cell voltage was measured at various current densities of 227, 246, 272, and 305 mAcm^{-2} , as shown in in Figure 5(a). When the cell was subjected to ~ 227 mAcm^{-2} for about 2 h, corresponding to a cell voltage of ~ +0.217 V, the cell voltage was stable and slightly increased, which might be due to the anode performance improvement associated with further reduction of NiO. Although the concentration polarization was slightly mitigated during the positive voltage test, a small increment in the current density (from 227 to 246 mAcm^{-2}) changed the cell voltage sign from positive to negative, implying that the concentration polarization resistance was still substantial. The performance of the bi-layer cell could be further improved by optimizing the anode microstructure. We believe that the non-optimized anode microstructure of the bi-layer cell would not affect the main experimental results (local electronic conduction in the electrolyte and the cell durability under negative voltage conditions) of the present study. Upon further increasing the current density from 246 ~ 305 mAcm^{-2} , the cell voltage decreased from -0.057 to -0.272 V. It can be seen that the cell voltage was stable under all operating conditions. After completing the tests, the cross-section of the bi-layer cell was examined by SEM, as shown in Figure 5(b), indicating there was neither delamination nor cracking at both the anode and cathode sides. These results contrasted with those of the BCY15-GDC20 and BZY15-NDC10 single layer cells, both of which showed a rapid voltage drop rate under similar test conditions [14]. Thus, we find that the cell stability under negative voltage conditions was greatly improved by utilizing the BCY15-GDC20 / BZY15-NDC10 bi-layer structure.

Three voltages were measured in the 'Pt probe embedded' bi-layer cell to elucidate how a bi-layer structure improved the cell stability. The voltage between the cathode and the anode (C-A), between 'Ref#1' and the anode (Ref#1-A) and between 'Ref#2' and the anode (Ref#2-A) was measured under open circuit conditions at 600°C, as shown in Figure 6. Initially, a mixture gas of 10% H₂ + balance N₂ gas was supplied for the reduction of NiO to Ni in the anode for ~ 30 min in which the three voltages were in a range of 0.2 ~ 0.4 V. After NiO reduction, 3% wet H₂ and air were supplied to the anode and cathode, respectively. The flow rates of 3% wet H₂ and air were fixed at 300 mLmin⁻¹. All three voltages increased upon supplying H₂ and air, but 'Ref#2-A' abruptly dropped to ~ 3 mV after ~ 2h H₂ supply. On the other hand, 'C-A' and 'Ref#1-A' were stabilized at voltage of 1.001 and 0.854 V, respectively. Note that the voltage of 'Ref#2-A' was as high as 0.2 ~ 0.4 V in 10% H₂ + balance N₂ (before H₂ supply), which means that 'Ref #2' and the anode were not physically shorted. The corresponding voltage variation through the Pt-Probe embedded bi-layer electrolyte is illustrated in Figure 7(a), where ϕ denotes the electric potential; we can see a small variation of ϕ in the regions close to the electrode interfaces, but a large variation in the middle region. Note that this type of voltage profile is quite different from that of the BCY15-GDC20 and the BZY15-NDC10 single layer cells [14]; the BCY15-GDC single layer cell showed a small ϕ change only in the region close to the anode side and the BZY15-NDC10 showed that only in the region close to the cathode side. With the designed bi-layer structure, electrolyte regions having a small ϕ variation were formed at both electrode sides. Note that an electrolyte region of a small ϕ change corresponds to a relatively low electronic resistance region.

The previous studies showed that local electronic conduction has a positive effect on both oxygen ionic and protonic SOFC stability under negative voltage conditions [34-36]. In the

following, we attempted to determine local electronic conductivities based on the ϕ variation measurement results in Figure 7(a). Since local electronic conduction is a function of atmosphere (partial pressure of oxygen or hydrogen) as well as dopant materials, temperature, etc., we needed information about the local internal partial pressures in the bi-layer electrolyte. Using voltage values of 'C-A', 'Ref#1-A', and 'Ref#2-A', we calculated the internal p_{O_2} in the corresponding regions. p_{O_2} at the positions of 'Ref#1' ($p_{O_2}^{Ref\#1}$) and 'Ref#2' ($p_{O_2}^{Ref\#2}$) can be written as Equation (2) and (3), respectively:

$$p_{O_2}^{Ref\#1} = p_{O_2}^A \times \exp\left[\frac{4e(\phi^{Ref\#1} - \phi^A)}{kT}\right] \quad (2)$$

$$p_{O_2}^{Ref\#2} = p_{O_2}^A \times \exp\left[\frac{4e(\phi^{Ref\#2} - \phi^A)}{kT}\right] \quad (3)$$

where k , e , and T are Boltzmann constant, elementary charge, and temperature, respectively; $\phi^{Ref\#1}$, $\phi^{Ref\#2}$, and ϕ^A are electric potentials at 'Ref#1', 'Ref#2', and the anode, respectively; $p_{O_2}^A$ is the oxygen partial pressure at the anode. The open circuit voltage was measured as ~ 1.001 V at 600°C , and we can assume that there was no significant electronic leakage through the bi-layer cell. Thus, the Nernst equation gave us $p_{O_2}^A \sim 1.61 \times 10^{-24}$ atm, and then $p_{O_2}^{Ref\#1}$ and $p_{O_2}^{Ref\#2}$ were determined as $\sim 8.48 \times 10^{-5}$ and $\sim 1.89 \times 10^{-24}$ atm, respectively, using Equation (2) and (3). The corresponding p_{O_2} variation through the bi-layer electrolyte is illustrated in Figure 7(b). The electrolyte region near the anode was in a very low oxygen partial pressure range of $\sim 10^{-24}$ atm while that near the cathode was in a relatively high oxygen partial pressure range of $8.48 \times 10^{-5} \sim 0.21$ atm. Using these p_{O_2} values, local electronic conductivities can be determined.

As mentioned above, the compositions of the bi-layer electrolyte regions near the anode and cathode interfaces were approximately the same as those of BCY15-GDC20 and BZY15-NDC10, respectively. According to [37, 38], the chemical and electrical properties of $\text{BaCe}_{0.85-x}\text{Zr}_x\text{Y}_{0.15}\text{O}_{3-d}$ approached those of BCY as x became smaller. Thus, it is a reasonable assumption that the electronic properties of BCY15-GDC20 and BZY15-NDC10 bar samples can represent the local electronic properties of the bi-layer electrolyte regions near the anode and cathode interfaces, respectively. It is well known that doped ceria exhibits n-type electronic conduction in a reducing atmosphere (at low p_{O_2}) even at 600 °C [39, 40]. BCY also consists of ceria and therefore we can expect a mixed ionic and electronic conduction in the BCY15-GDC20 composite under a reducing atmosphere. Although the electronic conductivity of BCY is smaller than its ionic conductivity, the electronic conduction cannot be neglected in a reducing atmosphere [30, 41-45]. The information about the electronic properties of BCY-GDC or a similar composite electrolyte is limited; most studies focused on the effect of the composite on the prevention of leakage current and the electrochemical performance [12, 13, 15, 16, 18-21]. According to Medvedev et al. [20], the electrical conductivity of the BCN (Nd doped barium cerate)-NDC composite (in 25:75 mol %) increased with decreasing p_{O_2} , at 600 °C. Although the molar ratio we employed in BCY15-GDC20 (in 50:50 mol %) is different, we can expect that ceria in the composite electrolyte is reduced in a low partial pressure range $< 10^{-20}$ atm. A bar sample of BCY15-GDC20 was prepared to determine its n-type conductivity. A four probe DC 4-probe conductivity was measured on the sample in various p_{O_2} . Electrical conductivities of the BCY15-GDC20 bar sample were measured in $p_{\text{O}_2} \sim 1.48 \times 10^{-23}$, $\sim 5.92 \times 10^{-25}$, and $\sim 1.51 \times 10^{-27}$ atm, and its plot as a function of $p_{\text{O}_2}^{-1/4}$ is shown in

Figure 8(a). Since it showed linear behavior, we used Equation (4) for estimating ionic and electronic conductivity of BCY15-GDC composite:

$$\sigma_t = \sigma_i + \sigma_e = \sigma_i + \sigma_e^0 \cdot (p_{O_2})^{-1/4} \quad (4)$$

where σ_t , σ_i , σ_e , and σ_e^0 are the total conductivity, ionic conductivity (considered approximately constant), n-type electronic conductivity at a given atmosphere, and n-type conductivity at $p_{O_2} = 1$ atm, respectively. From the plot, σ_i can be determined from the Y-axis intercept and σ_e^0 can be determined from the plot slope [19]. Note that σ_i and σ_e^0 include contributions from two materials, BCY and GDC. σ_i of the BCY15-GDC20 bar sample was $\sim 4.72 \times 10^{-3} \text{ Scm}^{-1}$, which is similar to the reported values of similar composite electrolytes at 600°C [12, 16-18, 20, 21]. Since the range of p_{O_2} in the anode side region ($p_{O_2}^A \sim p_{O_2}^{Ref\#2}$) was determined to be $1.61 \times 10^{-24} \sim 1.89 \times 10^{-24}$ atm by using embedded probes, we can calculate the electronic conductivity by $\sigma_e^0 \times p_{O_2}^{-1/4}$, which was $1.76 \times 10^{-3} \sim 1.84 \times 10^{-3} \text{ Scm}^{-1}$ in the corresponding region. Note that this value is similar to the increased electrical conductivity value of the BCN-NDC composite as decreasing from intermediate to low p_{O_2} , at 600°C [20].

The electrical conductivity of BZY increases with increasing p_{O_2} , developing p-type conduction, which was reported as $10^{-4} \sim 10^{-3} \text{ Scm}^{-1}$ in air at 600°C [46, 47]. We assumed that a solid solution was not formed in the BZY15-NDC10 region near the cathode side and therefore we can expect non-negligible p-type conduction near the cathode side. Similarly, a BZY-NDC bar sample was prepared and its electrical conductivities were measured in $p_{O_2} \sim 0.21, 0.5,$ and 0.99 atm. Figure 8(b) shows the corresponding conductivity plot as a function of $p_{O_2}^{1/4}$. The

linear behavior indicates that p-type conduction develops with increasing p_{O_2} . Since doped ceria is an almost pure ionic conductor in an oxidizing atmosphere [40], the increase in electrical conductivity with p_{O_2} should be due to p-type electronic conductivity from BZY. We can now determine p-type electronic conductivity of the electrolyte region near the cathode side using Equation (5):

$$\sigma_t = \sigma_i + \sigma_h = \sigma_i + \sigma_h^0 \cdot (p_{O_2})^{1/4} \quad (5)$$

where σ_t , σ_i , σ_h , and σ_h^0 are the total conductivity, ionic conductivity (considered approximately constant), p-type electronic conductivity at a given atmosphere, and p-type conductivity at $p_{O_2} = 1$ atm, respectively.. Similarly to Equation (4), σ_i can be determined from the Y-axis intercept and σ_h^0 can be determined from the plot slope [19]. σ_i of the BZY15-NDC10 was determined to be $\sim 9.3 \times 10^{-4} \text{ Scm}^{-1}$. Since the range of p_{O_2} in the cathode side region ($p_{O_2}^A \sim p_{O_2}^{Ref\#2}$) was determined to be $8.48 \times 10^{-5} \sim 0.21$ atm by using the embedded probes, we can calculate the p-type conductivity by $\sigma_h^0 \times p_{O_2}^{1/4}$, which was $3.33 \times 10^{-5} \sim 2.35 \times 10^{-4} \text{ Scm}^{-1}$ in the corresponding region. These values are somewhat lower than the reported p-type conductivity of pure BZY [46], but are much higher than electronic conductivity of an electrolyte with a high ionic transference number (e.g. p-type electronic conductivity $\sim 10^{-6} \text{ Scm}^{-1}$ of YSZ at 800°C) [48]. We can thus surmise that there is sufficient local electronic conduction established in the electrolyte regions close to both electrodes, which eventually plays a role in stabilizing the internal partial pressure, i.e., preventing electrode delamination [34, 49, 50]. The present results indicate that the bi-layer structure can be a practical solution to protect co-ionic conducting SOFCs in a cell-imbalanced stack.

IV. SUMMARY

In the present study, we modified the co-ionic conducting composite electrolyte design by utilizing a bi-layer structure: anode / BCY15–GDC20 / BZY15–NDC10 / cathode. The bi-layer cell was stable under both positive and negative voltage conditions, contrary to the single layered composite electrolyte cell. To understand the effects of the bi-layer structure on the stability, Pt probes were embedded in the bi-layer electrolyte for estimating the internal p_{O_2} . Using these values, n-type conductivity near the anode side ($\sim 10^{-3} \text{ Scm}^{-1}$) and p-type conductivity near the cathode side ($10^{-5} \sim 10^{-4} \text{ Scm}^{-1}$) were determined in combination with four probe DC conductivity measurements. The results indicate that local electronic conduction in electrolyte regions near both the anode and cathode interfaces is crucial for the durability of co-ionic conducting electrolytes under negative voltage operation. Thus, the bilayer structure is recommended for improving the stability of co-ionic conducting SOFCs in a cell imbalanced stack.

Acknowledgements: This work was supported by the National Research Foundation of Korea (NRF) grant funded by the Korea government (MSIT) (No. 2021R1A2C1003392) and (2021M313A1084830). This work was partly supported by Korea Institute of Energy Technology Evaluation and Planning (KETEP) grant funded by the Korean government (MOTIE) (No. 20213030030150). It was also supported in part by the U. S. Department of Energy under Grant Number DE-FG02-06ER46086.

REFERENCES

- [1] E.D. Wachsman, K.T. Lee, Lowering the temperature of solid oxide fuel cells, *Science*, 334 (2011) 935-939.
- [2] R.M. Ormerod, Solid oxide fuel cells, *Chem. Soc. Rev.*, 32 (2003) 17-28.
- [3] S.C. Singhal, K. Kendall, High-temperature solid oxide fuel cells: fundamentals, design and applications, Elsevier, 2003.
- [4] H. Yokokawa, H. Tu, B. Iwanschitz, A. Mai, Fundamental mechanisms limiting solid oxide fuel cell durability, *J. Power Sources*, 182 (2008) 400-412.
- [5] H. Yahiro, Y. Baba, K. Eguchi, H. Arai, High Temperature fuel cell with ceria-yttria solid electrolyte, *J. Electrochemical. Soc.*, 135 (1988) 2077.
- [6] Y. Zhang, J. Liu, M. Singh, E. Hu, Z. Jiang, R. Raza, F. Wang, J. Wang, F. Yang, B. Zhu, Superionic Conductivity in Ceria-Based Heterostructure Composites for Low-Temperature Solid Oxide Fuel Cells, *Nano-Micro Lett.*, 12 (2020) 1-20.
- [7] K. Venkataramana, C. Madhuri, C.V. Reddy, Triple-doped Ceria–Carbonate ($\text{Ce}_{0.8}\text{La}_{0.06}\text{Sm}_{0.06}\text{Gd}_{0.06}\text{O}_{2-\delta}$ – $(\text{Li–Na})_2\text{CO}_3$) nanocomposite solid electrolyte materials for LT–SOFC applications, *Ceram. Int.*, 46 (2020) 27584-27594.
- [8] L. Lei, J. Zhang, R. Guan, J. Liu, F. Chen, Z. Tao, Energy storage and hydrogen production by proton conducting solid oxide electrolysis cells with a novel heterogeneous design, *Energy Convers. Manag.*, 218 (2020) 113044.
- [9] K.-D. Kreuer, Proton-conducting oxides, *Annu. Rev. Mater. Res.*, 33 (2003) 333-359.
- [10] M.Y. Park, M.G. Jung, S.Y. Bae, H.-T. Lim, Correlation between internal chemical potential and durability of yttria-doped barium cerate (bcy)-based protonic ceramic fuel cells,

Electrochim. Acta, 204 (2016) 183-191.

[11] S.Y. Bae, J.-Y. Park, H.-T. Lim, Investigation of electronic transport property and durability of BCY-BZY electrolyte cells using embedded probes, *Electrochim. Acta*, 236 (2017) 399-407.

[12] J. Huang, L. Zhang, C. Wang, P. Zhang, CYO–BZCYO composites with enhanced proton conductivity: Candidate electrolytes for low-temperature solid oxide fuel cells, *Int. J. Hydrogen Energy*, 37 (2012) 13044-13052.

[13] Z. Gong, W. Sun, J. Cao, D. Shan, Y. Wu, W. Liu, $\text{Ce}_{0.8}\text{Sm}_{0.2}\text{O}_{1.9}$ decorated with electron-blocking acceptor-doped BaCeO_3 as electrolyte for low-temperature solid oxide fuel cells, *Electrochim. Acta*, 228 (2017) 226-232.

[14] A.K. Niaz, M.G. Jung, J.-Y. Park, A.V. Virkar, H.-T. Lim, Spatial investigation of electronic properties in composite electrolytes for solid oxide fuel cells using embedded probes, *J. Power Sources*, 438 (2019) 226945.

[15] W. Sun, Z. Shi, J. Qian, Z. Wang, W. Liu, In-situ formed $\text{Ce}_{0.8}\text{Sm}_{0.2}\text{O}_{2-\delta}$ @ $\text{Ba}(\text{Ce}, \text{Zr})_{1-x}(\text{Sm}, \text{Y})_x\text{O}_{3-\delta}$ core/shell electron-blocking layer towards $\text{Ce}_{0.8}\text{Sm}_{0.2}\text{O}_{2-\delta}$ -based solid oxide fuel cells with high open circuit voltages, *Nano Energy*, 8 (2014) 305-311.

[16] W. Sun, Y. Jiang, Y. Wang, S. Fang, Z. Zhu, W. Liu, A novel electronic current-blocked stable mixed ionic conductor for solid oxide fuel cells, *J. Power Sources*, 196 (2011) 62-68.

[17] B. Li, S. Liu, X. Liu, S. Qi, J. Yu, H. Wang, W. Su, Electrical properties of SDC–BCY composite electrolytes for intermediate temperature solid oxide fuel cell, *Int. J. Hydrogen Energy*, 39 (2014) 14376-14380.

[18] D. Lin, Q. Wang, K. Peng, L.L. Shaw, Phase formation and properties of composite

electrolyte $\text{BaCe}_{0.8}\text{Y}_{0.2}\text{O}_{3-\delta}$ - $\text{Ce}_{0.8}\text{Gd}_{0.2}\text{O}_{1.9}$ for intermediate temperature solid oxide fuel cells, *J. Power Sources*, 205 (2012) 100-107.

[19] D. Medvedev, V. Maragou, E. Pikalova, A. Demin, P. Tsiakaras, Novel composite solid state electrolytes on the base of BaCeO_3 and CeO_2 for intermediate temperature electrochemical devices, *J. Power sources*, 221 (2013) 217-227.

[20] D. Medvedev, E. Pikalova, A. Demin, A. Podias, I. Korzun, B. Antonov, P. Tsiakaras, Structural, thermomechanical and electrical properties of new $(1-x)\text{Ce}_{0.8}\text{Nd}_{0.2}\text{O}_{2-\delta}$ - $x\text{BaCe}_{0.8}\text{Nd}_{0.2}\text{O}_{3-\delta}$ composites, *Journal of Power Sources*, 267 (2014) 269-279.

[21] H. Wang, L. Zhang, X. Liu, H. Bi, S. Yu, F. Han, L. Pei, Electrochemical study on $\text{Ce}_{0.85}\text{Sm}_{0.15}\text{O}_{1.925}$ - $\text{BaCe}_{0.83}\text{Y}_{0.17}\text{O}_{3-\delta}$ composite electrolyte, *J. Alloys Compd.*, 632 (2015) 686-694.

[22] H.-H. Huang, H.-Y. Chen, K.-C. Liao, H.-T. Young, C.-F. Lee, J.-Y. Tien, Thermal-electrochemical coupled simulations for cell-to-cell imbalances in lithium-iron-phosphate based battery packs, *Appl. Therm. Eng.*, 123 (2017) 584-591.

[23] I. Zilberman, J. Schmitt, S. Ludwig, M. Naumann, A. Jossen, Simulation of voltage imbalance in large lithium-ion battery packs influenced by cell-to-cell variations and balancing systems, *J. Energy Storage*, 32 (2020) 101828.

[24] A.V. Virkar, A model for degradation of electrochemical devices based on linear non-equilibrium thermodynamics and its application to lithium ion batteries, *J. Power Sources*, 196 (2011) 5970-5984.

[25] M. Ghiji, V. Novozhilov, K. Moinuddin, P. Joseph, I. Burch, B. Suendermann, G. Gamble, A review of lithium-ion battery fire suppression, *Energies*, 13 (2020) 5117.

- [26] A.V. Virkar, A model for solid oxide fuel cell (SOFC) stack degradation, *J. Power Sources*, 172 (2007) 713-724.
- [27] H.-T. Lim, A.V. Virkar, A study of solid oxide fuel cell stack failure by inducing abnormal behavior in a single cell test, *J. Power Sources*, 185 (2008) 790-800.
- [28] B.-K. Park, Q. Zhang, P.W. Voorhees, S.A. Barnett, Conditions for stable operation of solid oxide electrolysis cells: oxygen electrode effects, *Energy Environ. Sci.*, 12 (2019) 3053-3062.
- [29] P. Wang, W. Qu, W.L. Song, H. Chen, R. Chen, D. Fang, Electro-chemo-mechanical issues at the interfaces in solid-state lithium metal batteries, *Adv. Funct. Mater.*, 29 (2019) 1900950.
- [30] M.G. Jung, Y.J. Kim, Y.-G. Jung, H.-T. Lim, Measurement of hydrogen and oxygen chemical potential in yttria doped barium cerate (BCY) electrolyte of anode-supported protonic ceramic fuel cells, *Int. J. Hydrogen Energy*, 39 (2014) 16576-16584.
- [31] K.D. Seo, Y.J. Kim, J.-y. Park, H.-T. Lim, Investigating the effect of current collecting conditions on solid oxide fuel cell (SOFC) performance with additional voltage probes, *Int. J. Hydrogen Energy*, 43 (2018) 2349-2358.
- [32] J. H. Joo, G. M. Choi, Open-circuit voltage of ceria-based thin film SOFC supported on nano-porous alumina, *Solid State Ionics*, 178 (2007) 1602-1607.
- [33] X. Zhang, M. Robertson, C. Deêes-Petit, W. Qu, O. Kesler, R. Maric, D. Ghosh, Internal shorting and fuel loss of a low temperature solid oxide fuel cell with SDC electrolyte, *J. Power Sources*, 164 (2007) 668-677.
- [34] L. Zhang, L. Zhu, A.V. Virkar, Modeling of oxygen chemical potential distribution in

solid oxide electrolyzer cells, *J. Electrochem. Soc.*, 166 (2019) F1275.

[35] M.J. Son, M.W. Kim, A.V. Virkar, H.-T. Lim, Locally developed electronic conduction in a yttria stabilized zirconia (YSZ) electrolyte for durable solid oxide fuel cells, *Electrochim. Acta*, 353 (2020) 136450.

[36] Y.J. Kim, H.-T. Lim, Improving the Stability of Series-Connected Solid Oxide Fuel Cells by Modifying the Electrolyte Composition, *J. Electrochem. Sci. Technol.*, 12 (2021) 159-165.

[37] P. Sawant, S. Varma, B. N. Wani, S. R. Bharadwaj, Synthesis, stability and conductivity of $\text{BaCe}_{0.8-x}\text{Zr}_x\text{Y}_{0.2}\text{O}_{3-\delta}$ as electrolyte for proton conducting SOFC, *Int. J. Hydrogen Energy*, 37 (2012) 3848-3856.

[38] K. Katahira, Y. Kohchi, T. Shimura, H. Iwahara, Protonic conduction in Zr-substituted BaCeO_3 , *Solid State Ionics*, 138 (2000) 91-98.

[39] T. Shimonosono, Y. Hirata, S. Sameshima, T. Horita, Electronic conductivity of La-doped ceria ceramics, *J. Am. Ceram. Soc.*, 88 (2005) 2114-2120.

[40] E. Souza, W. Chueh, W. Jung, E. Muccillo, S. Haile, Ionic and electronic conductivity of nanostructured, samaria-doped ceria, *J. Electrochem. Soc.*, 159 (2012) K127.

[41] I. Kosacki, J. Becht, R. Van Landschoot, J. Schoonman, Electrical properties of $\text{SrCe}_{0.95}\text{Yb}_{0.05}\text{O}_3$ in hydrogen containing atmospheres, *Solid State Ionics*, 59 (1993) 287-296.

[42] I. Kosacki, H. Tuller, Mixed conductivity in $\text{SrCe}_{0.95}\text{Yb}_{0.05}\text{O}_3$ protonic conductors, *Solid State Ionics*, 80 (1995) 223-229.

[43] A. Kruth, J.T. Irvine, Water incorporation studies on doped barium cerate perovskites, *Solid State Ionics*, 162 (2003) 83-91.

[44] S.-J. Song, E. Wachsman, S. Dorris, U. Balachandran, Defect Structure and n-Type

Electrical Properties of $\text{SrCe}_{0.95}\text{Eu}_{0.05}\text{O}_{3-\delta}$, *J. Electrochem. Soc.*, 150 (2003) A1484.

[45] A. Tomita, K. Tsunekawa, T. Hibino, S. Teranishi, Y. Tachi, M. Sano, Chemical and redox stabilities of a solid oxide fuel cell with $\text{BaCe}_{0.8}\text{Y}_{0.2}\text{O}_{3-\alpha}$ functioning as an electrolyte and as an anode, *Solid State Ionics*, 177 (2006) 2951-2956.

[46] S. Ricote, N. Bonanos, M.M. De Lucas, G. Caboche, Structural and conductivity study of the proton conductor $\text{BaCe}_{(0.9-x)}\text{Zr}_x\text{Y}_{0.1}\text{O}_{(3-\delta)}$ at intermediate temperatures, *J. Power Sources*, 193 (2009) 189-193.

[47] W. Wang, A.V. Virkar, Ionic and electron-hole conduction in $\text{BaZr}_{0.93}\text{Y}_{0.07}\text{O}_{3-\delta}$ by 4-probe dc measurements, *J. Power Sources*, 142 (2005) 1-9.

[48] T. Nakamura, K. Amezawa, J.r. Kulisch, W.G. Zeier, J.r. Janek, Guidelines for all-solid-state battery design and electrode buffer layers based on chemical potential profile calculation, *ACS Appl. Mater. Interfaces*, 11 (2019) 19968-19976.

[49] A.V. Virkar, Reversible fuel cells with tri-layer electrolytes, *ECS Trans.*, 68 (2015) 3253.

[50] A.V. Virkar, G. Tao, Reversible high temperature cells for power generation and hydrogen production using mixed ionic electronic conducting solid electrolytes, *Int. J. Hydrogen Energy*, 40 (2015) 5561-5577.

Captions

Figure 1: Schematic (a) and photograph (b) of anode supported bi-layer cell with two embedded probes.

Figure 2: (a) XRD patterns of BZY15, NDC10, BCY15, and GDC20 powders, and bi-layer electrolytes fired at 500°C and sintered 1550°C; (b) SEM image of the cross-section of a 'Pt probe free' bi-layer electrolyte sintered at 1550°C with EDS line scanning results of Zr.

Figure 3: SEM images of the cross section of the bi-layer electrolyte with Ref#1 (a) and Ref#2 (b).

Figure 4: Initial I-V-P curves (a) and impedance spectra (b) of the bi-layer electrolyte cell measured at 600°C.

Figure 5: (a) Voltage plot vs. time under positive voltage (+ 0.217 V) and negative voltage (- 0.057 ~ - 0.272 V) conditions, of the bi-layer cell at 600°C; (b) SEM image of the bi-layer cell after tests.

Figure 6: The voltage between the cathode and anode (C-A), between 'Ref#1' and the anode (Ref#1-A) and between 'Ref#2' and the anode (Ref#2-A) measured under open circuit conditions at 600°C; the anode gas was changed from 10% H₂ + N₂ to 3% wet H₂ at ~ 0.5 h.

Figure 7: ϕ (a) and p_{O_2} (b) variation through the Pt probe embedded bi-layer electrolyte at 600°C under open circuit conditions.

Figure 8: Electrical conductivity measurements on the BCY15-GDC20 bar sample as a function of $p_{O_2}^{-1/4}$ (a) and the BZY15-NDC10 bar sample as a function of $p_{O_2}^{1/4}$ (b), at 600°C.

Figures

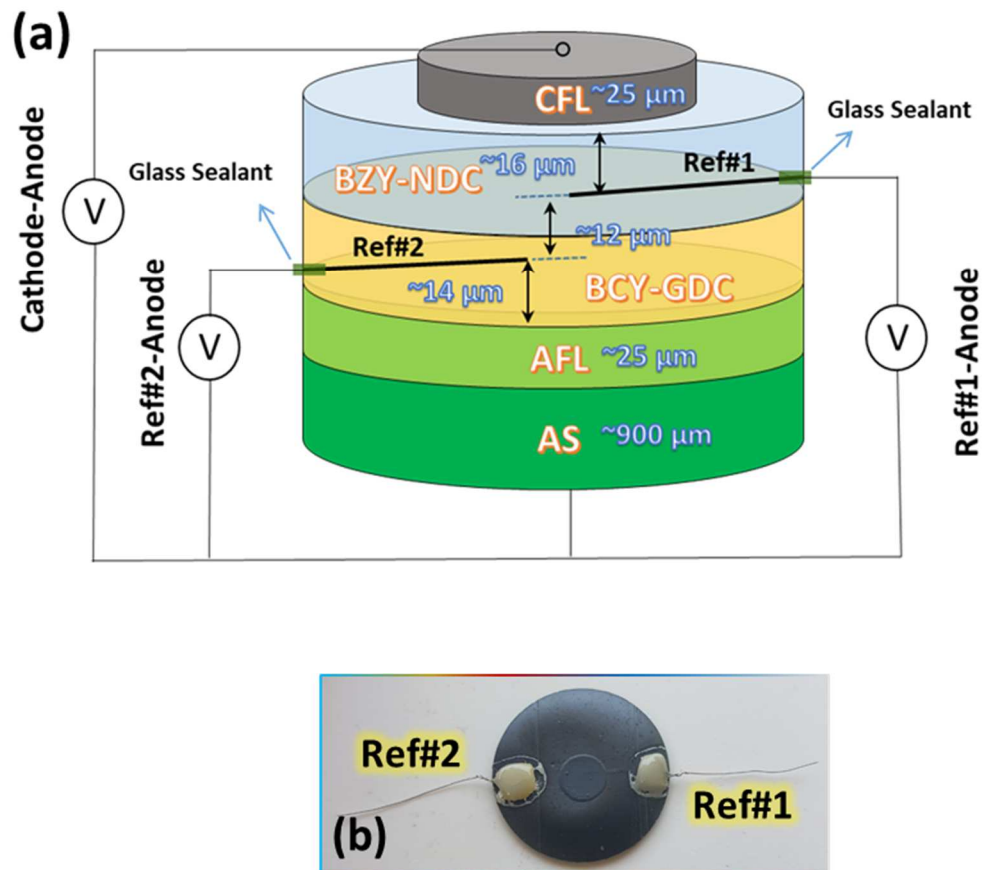


Figure 1: Schematic diagram (a) and photograph (b) of anode supported bi-layer cell with two embedded probes

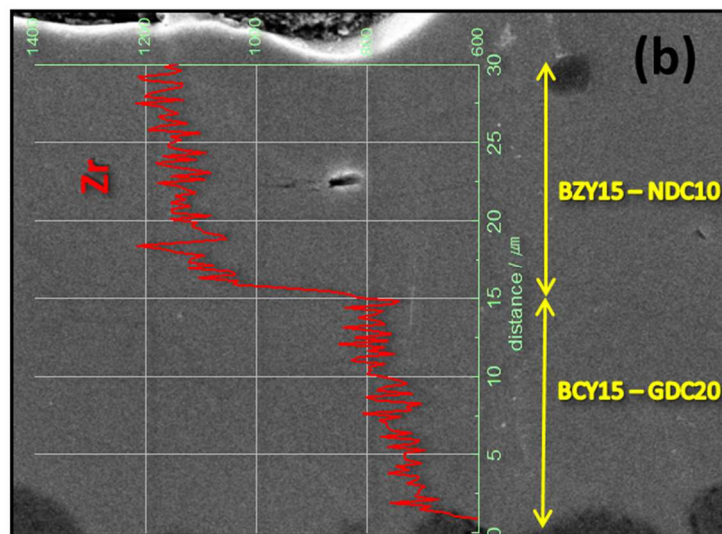
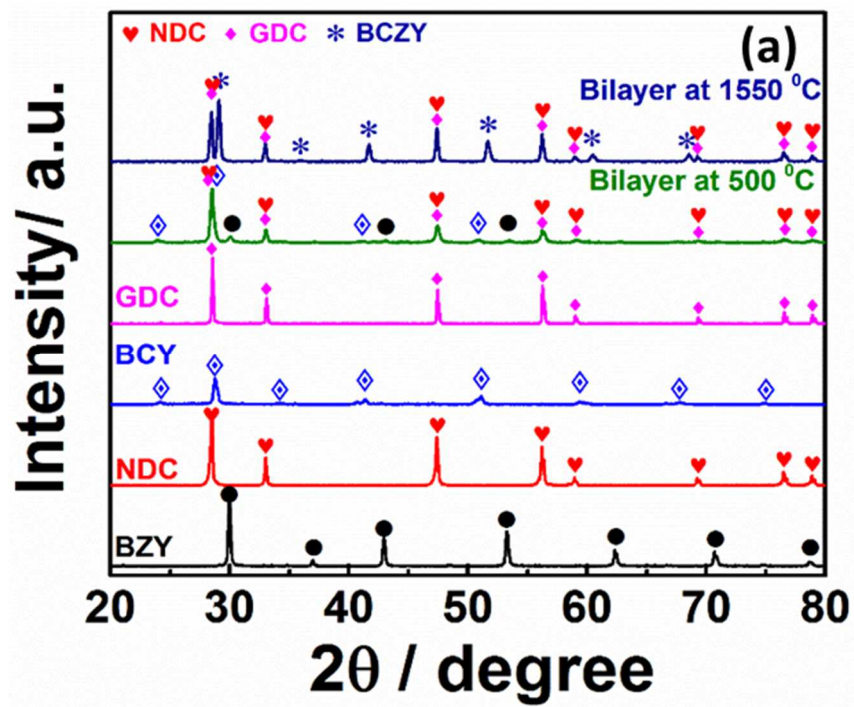


Figure 2: (a) XRD patterns of BZY15, NDC10, BCY15 and GDC20 powders, and bi-layer electrolytes fired at 500°C and sintered 1550°C; (b) SEM image of the cross-section of a 'Pt probe free' bi-layer electrolyte sintered at 1550°C with EDS line scanning results of Zr.

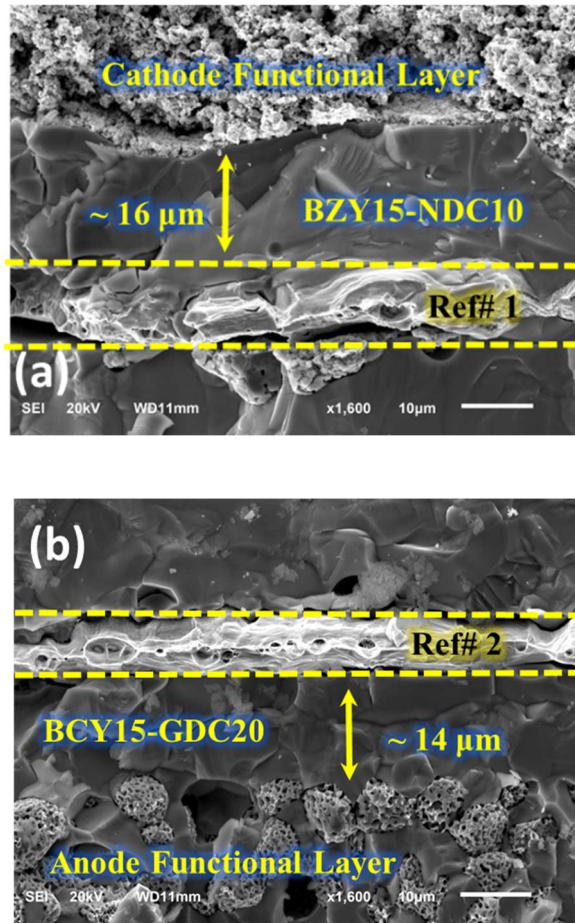


Figure 3: SEM images of the cross section of the bi-layer electrolyte with Ref#1 (a) and Ref#2 (b).

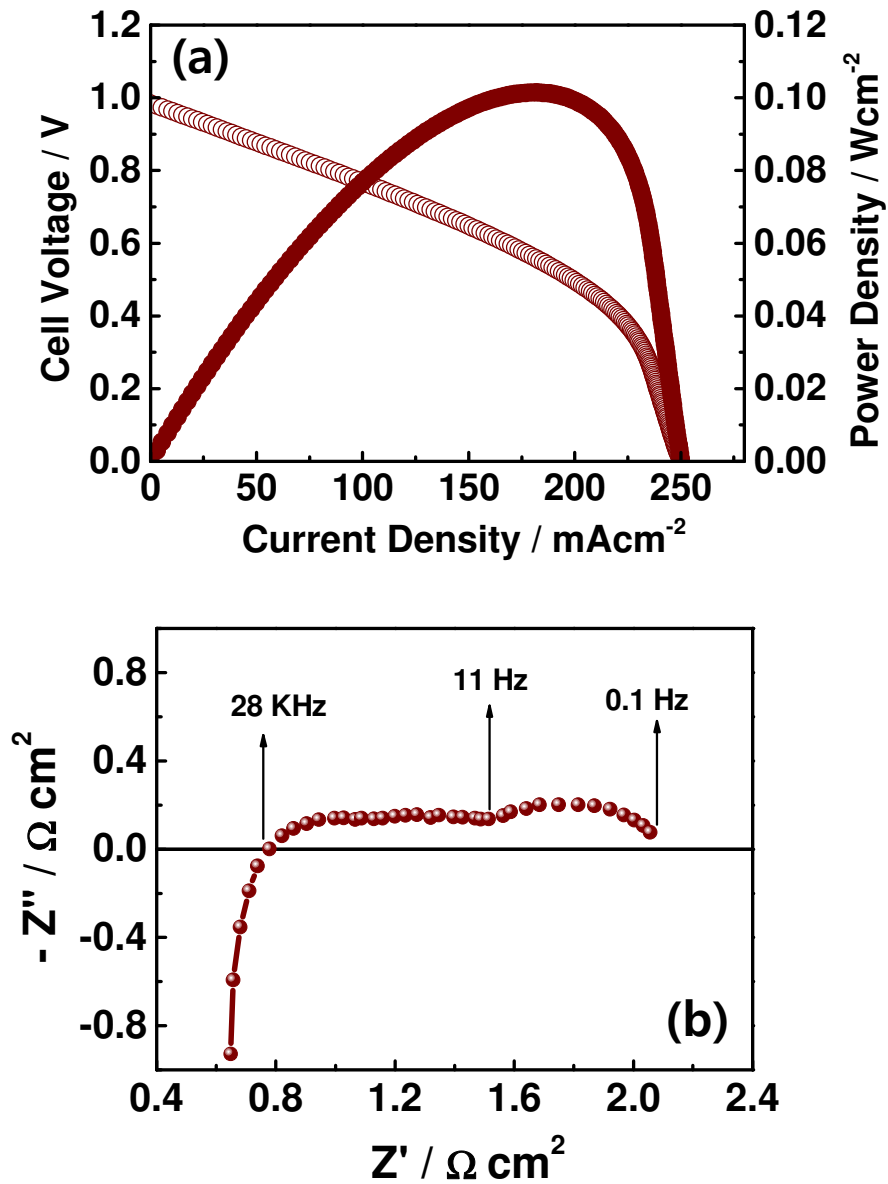


Figure 4: Initial I-V-P curves (a) and impedance spectra (b) of the bi-layer electrolyte cell measured at 600°C.

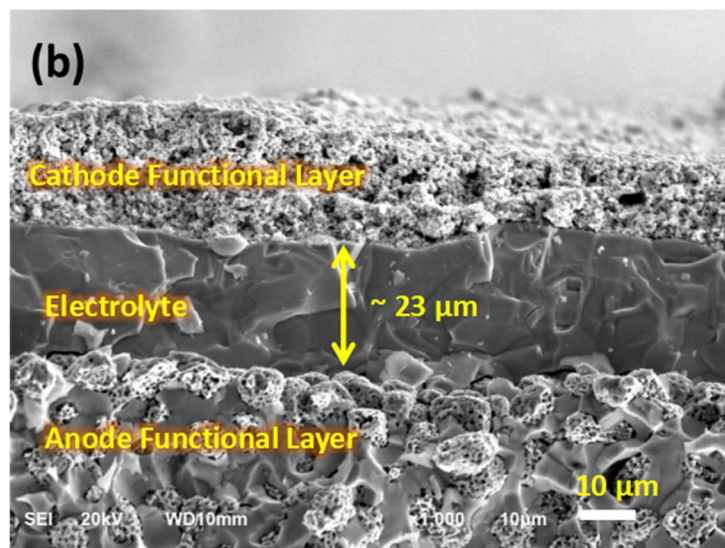
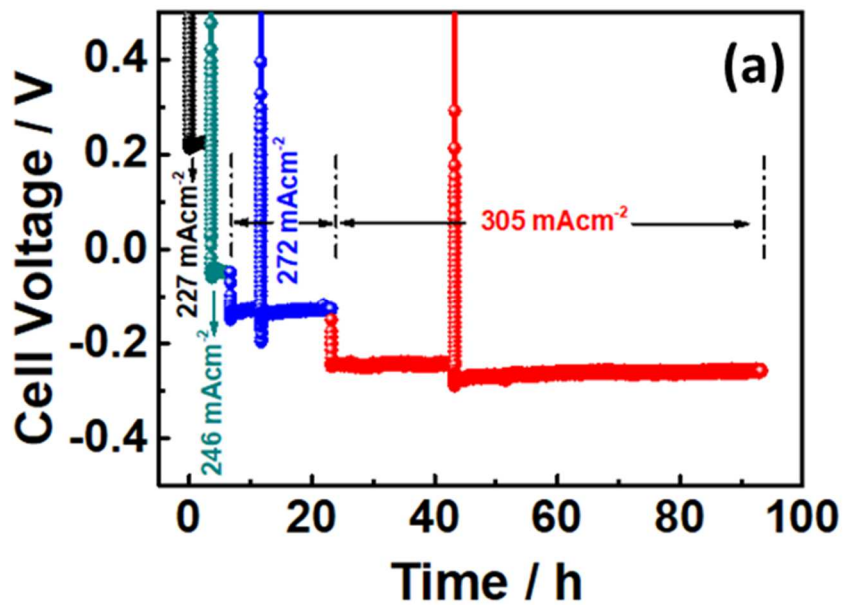


Figure 5: (a) Voltage plot vs. time under positive voltage (+ 0.217 V) and negative voltage (- 0.057 ~ - 0.272 V) conditions, of the bi-layer cell at 600°C; (b) SEM image of the bi-layer cell after tests.

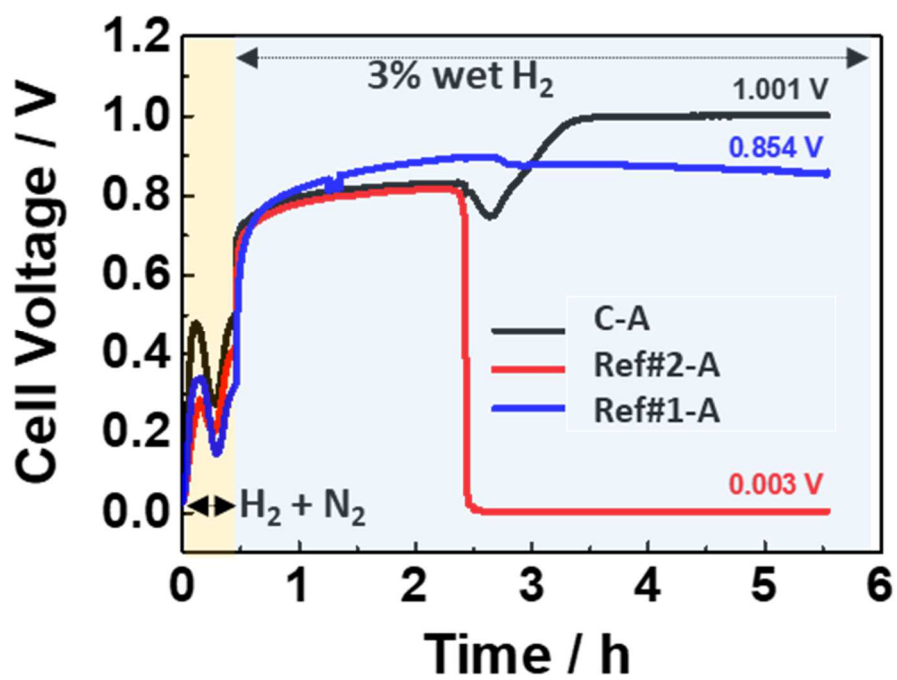


Figure 6: The voltage between the cathode and the anode (C-A), between 'Ref#1' and the anode (Ref#1-A) and between 'Ref#2' and the anode (Ref#2-A) measured under open circuit conditions at 600°C; the anode gas was changed from 10% H₂ + N₂ to 3% wet H₂ at ~ 0.5 h.

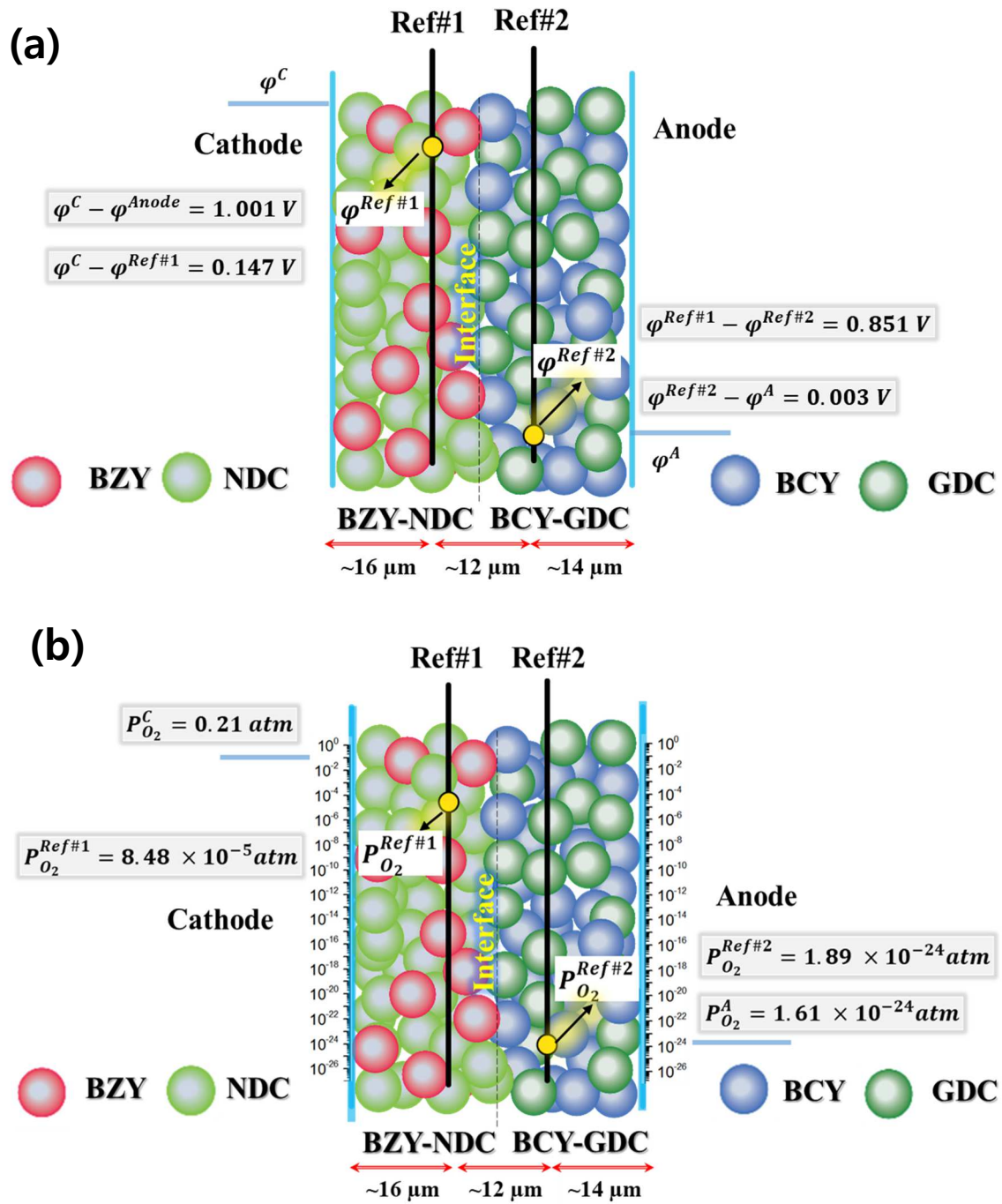


Figure 7: ϕ (a) and p_{O_2} (b) variation through the Pt probe embedded bi-layer electrolyte at 600°C under open circuit conditions.

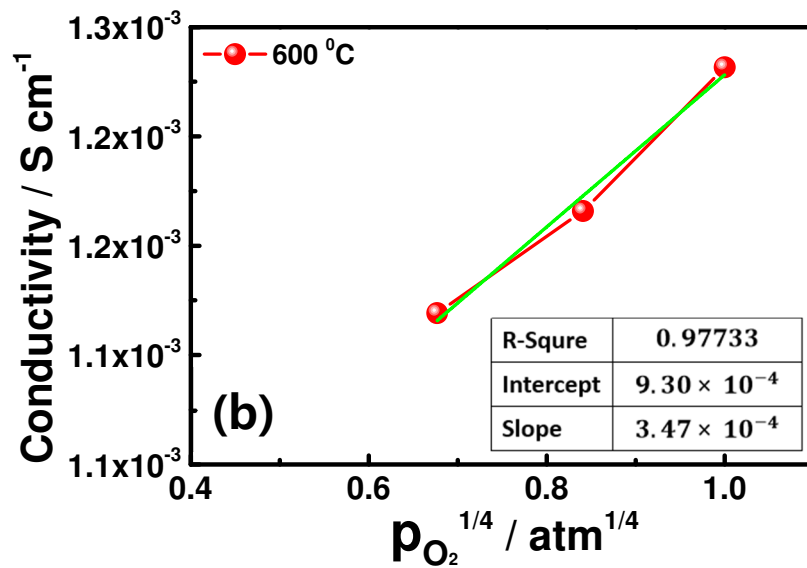
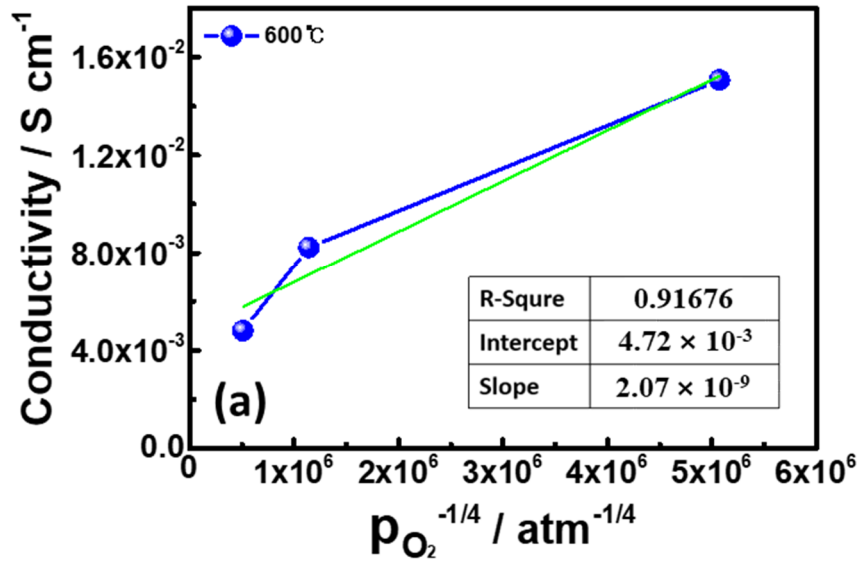


Figure 8: Electrical conductivity measurements on the BCY15-GDC20 bar sample as a function of $p_{O_2}^{-1/4}$ (a) and the BZY15-NDC10 bar sample as a function of $p_{O_2}^{1/4}$ (b), at 600°C.

P-type conduction
 $10^{-5} \sim 10^{-4} \text{ Scm}^{-1}$

